Miettinen, Mikael; Vainio, Valtteri; Viitala, Raine

Aerostatic porous annular thrust bearings as seals

Published in:
Tribology International

DOI:
10.1016/j.triboint.2024.110073

Published: 01/12/2024

Document Version
Publisher's PDF, also known as Version of record

Please cite the original version:
Miettinen, M., Vainio, V., & Viitala, R. (2024). Aerostatic porous annular thrust bearings as seals. *Tribology International*, *200*, Article 110073. https://doi.org/10.1016/j.triboint.2024.110073

Tribology International 200 (2024) 110073

Contents lists available at ScienceDirect

Tribology International

journal homepage: www.elsevier.com/locate/triboint

Full Length Article

Aerostatic porous annular thrust bearings as seals

Mikael Miettinen *, Valtteri Vainio, Raine Viitala

Department of Mechanical Engineering, Aalto University, Espoo, Finland

ARTICLE INFO

Keywords:
Gas lubrication
Externally pressurized
Non-contact seal
Porous restrictor

ABSTRACT

Externally pressurized porous thrust bearings can be used for simultaneous sealing and bearing functions. Performance characterizing metrics of aerostatic seals include load capacity, stiffness, air consumption and leakage. Gas flow in porous aerostatic bearings and seals can be modeled using modified Reynolds equation, where a porous feeding term is included. In this paper, a non-dimensional analytical solution for the pressure distribution is proposed for annular thrust seals with assumption of one-dimensional restrictor flow. It is shown, that the analytic solution is equivalent to a numerical solution with two-dimensional restrictor flow on the most significant performance metrics under static conditions. The theoretical results are validated by experiments with two 64 mm diameter aerostatic graphite seals, demonstrating the accuracy of the proposed models.

1. Introduction

Non-contact sealing is common in high-speed machinery and precision applications, where minimal friction in the seal is desirable. Due to the inherent gap in non-contact seals, some leakage exists through the seal gap. This leakage can be mitigated, for example, by introducing a sealing gas supply to the gap, as is done in aerostatic seals. The sealing gas can be any gas, such as air or an inert gas, which is used in processes where the introduction of oxygen is undesirable. The sealing gas inhibits flow from the high-pressure side to the low-pressure side of the seal by introducing a even higher pressure region into the seal gap. Consequently, a portion of the sealing gas leaks to the high pressure side and to the ambient.

Porous annular thrust seals with additively manufactured restrictors for turbomachinery have been investigated by Schoar et al. [1–4]. Stainless steel restrictors with varying permeability were manufactured and investigated numerically and experimentally. The seal was preloaded against the guide surface with the supply pressure of the seal, and the seal air gap pressure was measured with multiple holes in the guide surface.

Aerostatically sealed volumes as load generating machine elements under dynamic conditions have been investigated experimentally by the authors [5]. Only the total load capacity, air consumption, and friction was investigated, omitting measurements of the seal air gap height. Further, static performance of annular thrust seals and circular thrust bearings was experimentally and numerically investigated [6]. Numerical model with uni-axial restrictor flow was used and the results were published in dimensional form, limiting the applicability of the results.

In addition to research on aerostatic seals, aerostatic bearing research is relevant due to the similarities in materials, designs, and operation. In particular, studies on annular thrust bearings and studies on restrictor materials and modeling hold high relevance to annular seals, as the main difference between seals and bearings is the existence of a pressure differences across a seal. A multitude of theoretical and experimental studies on porous annular thrust bearings have been conducted, for example, in [7–10].

The permeability of the porous restrictor is a key parameter influencing the performance of an aerostatic porous seal or a bearing. Typically, the porous restrictor has been modeled with Darcy's law [11, 12]. Numerous studies have made comparisons of linear and nonlinear Darcy's law for modeling of the restrictor with numerical 1D and 3D models, including experimental validations with various bearing geometries [13–17]. More recently, elaborate permeability models for modeling of the flow through the porous restrictor have been proposed [18–23]. Additionally, partially porous rectangular and axisymmetric bearings have been numerically analyzed [24,25]. Further, the crash resilience of the restrictor materials and design has been investigated from reliability [26] and performance [27] perspectives.

Phenomena at the interface between the porous restrictor and the flow in the air gap has been investigated in multiple studies. The existence of a slip condition at the boundary of a narrow channel and a porous wall, i.e., the air gap and restrictor of aerostatic seal or a bearing, was identified and investigated by [28–33]. Further, dynamic squeeze film effects of annular porous surfaces, as in annular thrust bearings have been investigated [34,35]. More recently, the effect of

* Corresponding author.
E-mail address: mikael.miettinen@aalto.fi (M. Miettinen).

https://doi.org/10.1016/j.triboint.2024.110073
Received 26 June 2024; Received in revised form 25 July 2024; Accepted 5 August 2024
Available online 6 August 2024

the slip on the performance of thrust and journal bearings has been investigated experimentally and numerically [16,36].

Analytical solutions for aerostatic bearings with some particular geometries have been derived by, for example, Constantinescu [37], Sun [38], Murti [39], Murti [40] and Sun [41]. The geometries include axis-symmetric circular and annular thrust, conical, spherical and infinitely long rectangular bearings. These solutions have been shown to provide reasonable accuracy under static conditions by experimental validation [11]. However, similar analytical solutions for aerostatic seals have not yet been presented.

In this paper, it is shown, that an exact analytical solution exists for the modified Reynolds equation for annular aerostatic seals. The analytical solution requires the assumption of purely vertical flow in the porous restrictor. However, the slip coefficient of Goldstein and Braun [29] and Beavers et al. [28] can be applied. The analytical solution is compared to experiments and a numerical model with two dimensional flow in the restrictor.

Furthermore, the static performance of aerostatic axis-symmetric seals is investigated. The results are presented in non-dimensional form. A seal specific normalization is used, relating the performance parameters to the area of the porous restrictor. The proposed normalization better decouples the results from the variation of the ratio of the inner and outer radius of the seal.

The authors claim the following original contributions:

1. Closed-form solution for pressure distribution in a porous annular aerostatic face seal including slip effects.
2. Numerical model of pressure distribution of a porous annular aerostatic thrust seal including slip effects and feed geometry.
3. A proposal for normalization scheme for porous aerostatic seals.
4. Simulation study of seal performance based on the derived analytical solution and numerical model of static performance of aerostatic annular thrust seals with experimental verification of the theoretical results.

This paper is structured as follows: theoretical model of the aerostatic seal is introduced in Section 2, the experimental setup and procedure are described in Section 3, the theoretical and experimental results are presented and discussed in Section 4, and finally, some conclusions are drawn in Section 5.

2. Seal model

The investigated axisymmetric annular seal was modeled analytically and numerically. A cross-section of the investigated seal is presented in Fig. 1. Analytical models considered one dimensional flow in the air gap and restrictor, while the numerical model considered two dimensional flow in the restrictor and one dimensional flow in the air gap.

The domains of the analytical and numerical models are presented in 2. The flow in the air gap of both solutions is modeled with the Reynolds equation. In the analytical solution, the flow in the porous restrictor is assumed one dimensional, i.e., purely vertical. In the numerical model with slip at the restrictor-gap interface, two dimensional flow in the restrictor is assumed. Thus, the effect of the position and width of the supply grooves is be included in the numerical model, while the analytical model assumes that the whole top surface of the restrictor is subjected to the supply pressure. Additionally, back flow into the restrictor from the air gap is possible in both models, as increasing chamber pressure to higher than the supply pressure leads to reversal of the flow direction.

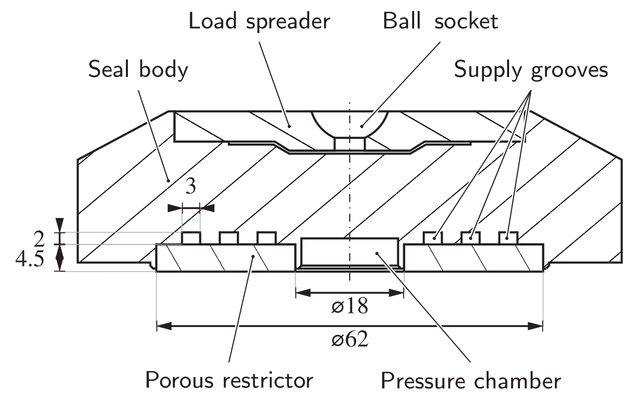

Fig. 1. Features and main dimensions of investigated seal.

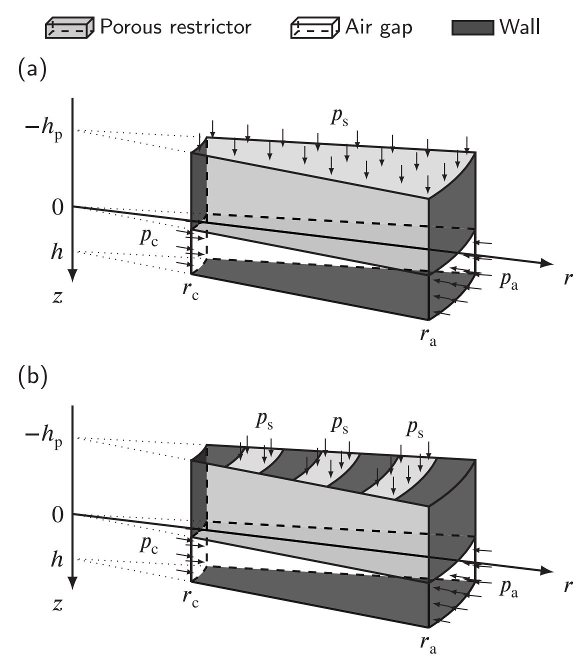

Fig. 2. Domain and boundary conditions of analytical model (a) and numerical model (b). h is height of air gap, h_p is height of porous restrictor, p is pressure at boundary and r is radius with indices: s supply, a ambient and c chamber. Flow in porous restrictor is purely vertical in analytical model and two dimensional in numerical model.

2.1. Nondimensional parameters

Normalization of the design parameters allows generalization of the problem and simplifies analysis by reducing the number of design parameters. Commonly, in research of aerostatic bearings and seals, the variables are nondimensionalized according to the ambient conditions. Thus, dimensionless variables are used in this study. The variables are normalized in relation to the conditions at the exit to the ambient at the outer radius of the seal and the surface area of the seal face. Dimensionless variables are represented with upper case symbols while dimensional variables are represented with lower case symbols, with the exception of the dimensionless porous feeding number β.

Pressures are normalized in relation to the ambient pressure p_a. Radial lengths are normalized in relation to the outer radius of the seal r_a. Vertical lengths in the air gap are normalized in relation to the air gap height h at the outer radius, and in the restrictor in relation to the height of the restrictor h_p at the outer radius. However, in the present study, both of these heights are uniform, i.e., nondimensional heights H, H_p are equal to 1. Additionally, the commonly used porous feeding number β is used for the nondimensionalization of the permeability effects of the porous restrictor [8,37]. Load capacity, static stiffness and flow rates are nondimensionalized in relation to the seal surface area $A = \pi(r_a{}^2 - r_c{}^2)$. The nondimensionalizations used in the present study are as follows:

$$\begin{aligned} \boldsymbol{R} &= \frac{\boldsymbol{r}}{r_a} \\ \boldsymbol{P}(R) &= \frac{\boldsymbol{p}(r)}{p_a} \\ \beta &= \frac{6\kappa r_a{}^2}{h_p h^3} \\ W &= \frac{w}{\pi\left(r_a{}^2 - r_c{}^2\right)p_a} \\ K &= \frac{kh}{\pi\left(r_a{}^2 - r_c{}^2\right)p_a} \\ \dot{\boldsymbol{M}}(R) &= \frac{\dot{\boldsymbol{m}}(r)\mu h_p}{\pi\left(r_a{}^2 - r_c{}^2\right)\rho k p_a} \end{aligned} \tag{1}$$

where $\boldsymbol{R}$ and $\boldsymbol{r}$ are radial positions, $\boldsymbol{P}(R)$ and $\boldsymbol{p}(r)$ are pressure in the air gap, W and w are load capacity, K and k are static stiffness, $\dot{\boldsymbol{M}}(R)$ and $\dot{\boldsymbol{m}}(r)$ are mass flows. Seal supply $\dot{M}_s$, chamber $\dot{M}_c$ and ambient $\dot{M}_a$ mass flows, were nondimensionalized in the same way for the sake of comparability of the flow rates.

The nondimensional performance parameters were calculated as follows: Load capacity of a seal can be numerically integrated from the pressure distribution in the air gap:

$$W = \int_{R_c}^{R_a} \boldsymbol{P}\,\mathrm{d}R. \tag{2}$$

Static stiffness of a seal is:

$$K = \frac{\partial W}{\partial h}h. \tag{3}$$

Mass flow in the air gap is:

$$\dot{\boldsymbol{M}}(R) = \frac{\boldsymbol{R}}{2\beta}\frac{\partial \boldsymbol{P}^2}{\partial R}. \tag{4}$$

Thus, the mass flows $\dot{M}_s$ from the seal supply, $\dot{M}_c$ into the chamber, and $\dot{M}_a$ into the ambient are:

$$\begin{aligned} \dot{M}_c &= \dot{\boldsymbol{M}}(R_c) \\ \dot{M}_a &= \dot{\boldsymbol{M}}(R_a) \\ \dot{M}_s &= \dot{M}_c + \dot{M}_a \end{aligned} \tag{5}$$

2.2. Governing equations

The fluid flow in a porous restrictor of an aerostatic seal or bearing is commonly described using the Darcy's law [12,42]. The Darcy's equation relates the flow rate in a porous material to the permeability of the material. Substituting the flow rate into the continuity equation, following equation for the pressure $\boldsymbol{P}_p$ in the porous restrictor under static and isothermal conditions is obtained [8]:

$$\nabla^2 \boldsymbol{P}_p{}^2 = 0. \tag{6}$$

where $\boldsymbol{P}_p$ is the nondimensional pressure in the porous restrictor. The permeability of the restrictor, κ is assumed constant, and thus can be included in the porous feeding parameter β, which is included in the equation for the air gap domain.

Modified Reynolds equation for porous aerostatic bearings and seal, in dimensionless form [9,11,37,43]:

$$\boldsymbol{\nabla}\cdot\left((1+\Phi)\boldsymbol{P}H^3\boldsymbol{\nabla}\boldsymbol{P}\right) = \beta\left.\frac{\partial \boldsymbol{P}_p{}^2}{\partial Z}\right|_{Z=0} \tag{7}$$

where

$$\begin{aligned} \Phi &= \frac{3SH + 6\alpha^2 S^2}{H\left(S^2 + H\right)} \\ S &= \frac{\sqrt{\kappa}}{\alpha h_a} \end{aligned} \tag{8}$$

In which β is dimensionless porous feeding parameter that is dependent on the permeability of the porous material κ, outer radius of the seal r_a, thickness of the porous material h_p, and air gap height at the ambient h_a. Φ is a dimensionless parameter accounting for slip at the porous surface, that utilizes the dimensionless slip parameter S defined by Goldstein and Braun [29]. α is a material specific slip coefficient. Slip coefficient α of 0.1 was used in the present study, as has been previously used with graphite restrictors of similar permeability [8,9]. The slip coefficient is an experimentally determined coefficient and its quantification is tedious. Selection of different slip parameters have been compared by Luong et al. [16].

2.3. Analytical solution

Analytical solutions have been presented for some primitive bearing geometries with appropriate assumptions, such as an axisymmetric and infinitely long rectangular bearings [11,37]. Analytical solutions require further simplifications to the flow in the porous restrictor. The analytical solution presented in this research assumes unidirectional flow in z-direction in the porous restrictor, as the thickness of the porous material is commonly small compared to its width, the pressure gradient in the porous feeding term simplifies to:

$$\left.\frac{\partial \boldsymbol{P}_p{}^2}{\partial Z}\right|_{Z=0} = -\left(P_s{}^2 - \boldsymbol{P}^2\right) \tag{9}$$

With assumptions of uniform gap height ($h = constant$, thus $H = 1$) and substituting $\boldsymbol{\Pi} = \boldsymbol{P}^2$, Eq. (7) reduces to [11]:

$$(1+\Phi)\nabla^2\boldsymbol{\Pi} = -2\beta(P_s{}^2 - \boldsymbol{\Pi}) \tag{10}$$

Written in cylindrical coordinates:

$$\frac{1}{\boldsymbol{R}}\frac{\partial}{\partial R}\left(\boldsymbol{R}\frac{\partial \boldsymbol{\Pi}}{\partial R}\right) = -\frac{2\beta}{1+\Phi}(P_s{}^2 - \boldsymbol{\Pi}). \tag{11}$$

Which is a zero-order Bessel differential equation. Thus, its has a solution in the form [37]:

$$\boldsymbol{\Pi}(R) = C_1 I_0\left(\sqrt{\frac{2\beta}{1+\Phi}}\boldsymbol{R}\right) + C_2 K_0\left(\sqrt{\frac{2\beta}{1+\Phi}}\boldsymbol{R}\right), \tag{12}$$

where I_0 and K_0 are modified Bessel functions of the first and the second kind, respectively. The integration coefficients C_1 and C_2 can be solved from the boundary conditions:

$$\begin{aligned} \boldsymbol{P}(R_c) &= P_c \\ \boldsymbol{P}(R_a) &= P_a \end{aligned} \tag{13}$$

where P_c is the chamber pressure and P_a is the ambient pressure. Thus, a closed form solution to the pressure distribution in an annular seal including slip effects is:

$$\boldsymbol{P}(R) = \sqrt{P_s{}^2 - C_1 I_0(\beta_s \boldsymbol{R}) + C_2 K_0(\beta_s \boldsymbol{R})}, \tag{14}$$

β_s is porous feeding term β adjusted with the slip factor Φ. The coefficients C_1, C_2 and β_s are

$$\begin{aligned} C_1 &= \frac{\left(P_s{}^2 - P_c{}^2\right)I_0(\beta_s R_a) + \left(P_a{}^2 - P_s{}^2\right)I_0(\beta_s R_c)}{I_0(\beta_s R_c)K_0(\beta_s R_a) - K_0(\beta_s R_c)I_0(\beta_s R_a)} \\ C_2 &= \frac{\left(P_c{}^2 - P_s{}^2\right)K_0(\beta_s R_a) + \left(P_s{}^2 - P_a{}^2\right)K_0(\beta_s R_c)}{K_0(\beta_s R_c)I_0(\beta_s R_a) - I_0(\beta_s R_c)K_0(\beta_s R_a)} \\ \beta_s &= \sqrt{\frac{2\beta}{(1+\Phi)}}. \end{aligned} \tag{15}$$

2.4. Numerical solution

A numerical solution including the slip effects and two dimensional flow in the porous restrictor is presented. The pressure in the porous restrictor and the pressure in the air gap are solved with a finite

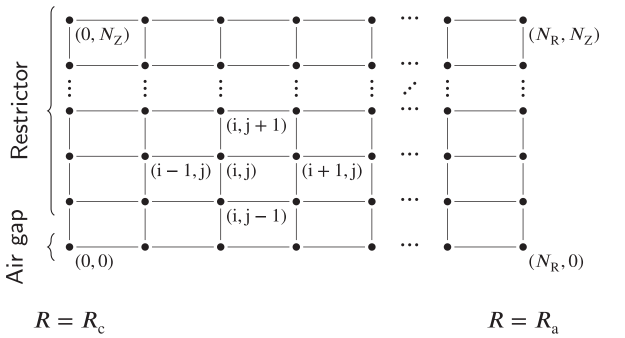

Fig. 3. Discretization of the domain of the investigated aerostatic seal. The mesh consist of $N_R \times N_Z$ nodes. A five-point stencil was used in the discretization. Boundary conditions are included into the nodes at the outer edges of the restrictor and at the inner and outer radius of the air gap.

difference method. The discretization of the domain is presented in Fig. 3.

Eq. (6) for pressure distribution in the porous restrictor, transformed into cylindrical coordinates:

$$\frac{1}{\boldsymbol{R}}\frac{\partial}{\partial R}\left(\boldsymbol{R}\frac{\partial \boldsymbol{P}_{\mathrm{p}}{}^{2}}{\partial R}\right)+\frac{\partial^{2}\boldsymbol{P}_{\mathrm{p}}{}^{2}}{\partial Z^{2}}=0 \tag{16}$$

Eq. (7) for air gap in cylindrical coordinates:

$$\frac{1}{\boldsymbol{R}}\frac{\partial}{\partial R}\left((1+\boldsymbol{\Phi})\boldsymbol{R}H^{3}\frac{\partial \boldsymbol{P}^{2}}{\partial R}\right)=2\beta\left.\frac{\partial \boldsymbol{P}_{\mathrm{p}}{}^{2}}{\partial Z}\right|_{Z=0} \tag{17}$$

Boundary conditions for the supply grooves of the porous restrictor are

$$\boldsymbol{P}_{\mathrm{p}}(R_{\mathrm{groove}},1)=P_{\mathrm{s}}, \tag{18}$$

and boundary conditions for the walls of the porous restrictor are

$$\frac{\partial}{\partial R}\boldsymbol{P}_{\mathrm{p}}(R_{\mathrm{wall}},1)=0 \qquad \frac{\partial}{\partial R}\boldsymbol{P}_{\mathrm{p}}(R_{\mathrm{c}},Z)=0 \qquad \frac{\partial}{\partial R}\boldsymbol{P}_{\mathrm{p}}(R_{\mathrm{a}},Z)=0. \tag{19}$$

Substituting $P_{i,j}^2 = \Pi_{i,j}$ into Eq. (17) and applying the boundary conditions, the discretization for the porous domain ($j > 0$) is

$$\frac{(R_{i,j}+R_{i-1,j})\Pi_{i-1,j}-(R_{i+1,j}+2R_{i,j}+R_{i-1,j})\Pi_{i,j}+(R_{i,j}+{}_{i+1,j})\Pi_{i+1,j}}{2R_{i,j}\Delta R^{2}} + \frac{\Pi_{i,j-1}+2\Pi_{i,j}+\Pi_{i,j+1}}{2\Delta Z^{2}}=F_{i,j} \tag{20}$$

and the discretization for the air gap domain ($j = 0$) is

$$(1+\Phi)H^{3}\frac{(R_{i,1}+R_{i-1,1})\Pi_{i-1,1}-(R_{i+1,1}+2R_{i,1}+R_{i-1,1})\Pi_{i,1}+(R_{i,1}+R_{i+1,1})\Pi_{i+1,1}}{4R_{i,1}\Delta R^{2}} - \beta\frac{\Pi_{i,1}-\Pi_{i,2}}{\Delta Z}=F_{i,1} \tag{21}$$

The discretized equation is solved for $\boldsymbol{\Pi}$, giving the pressure distribution in the seal gap and in the restrictor.

3. Experiment

The results of the model were verified with experiments. Two annular thrust seals with graphite restrictors were used in the investigations. The permeability of the restrictor was measured with the short circuit flow method [12]. Substituting ideal gas law into the Darcy's law, an expression for permeability κ of the restrictor is obtained:

$$\kappa=\frac{2\mu h_{\mathrm{p}}p_{\mathrm{s}}q_{\mathrm{s}}}{\pi({r_{\mathrm{a}}}^{2}-{r_{\mathrm{c}}}^{2})({p_{\mathrm{s}}}^{2}-{p_{\mathrm{a}}}^{2})}, \tag{22}$$

where μ is the dynamic viscosity of air, q_s is the supply flow rate, h_p is the height of the restrictor, r_c and glsr2 are inner and outer radius of the restrictor, p_s is the supply pressure and p_a is the ambient pressure.

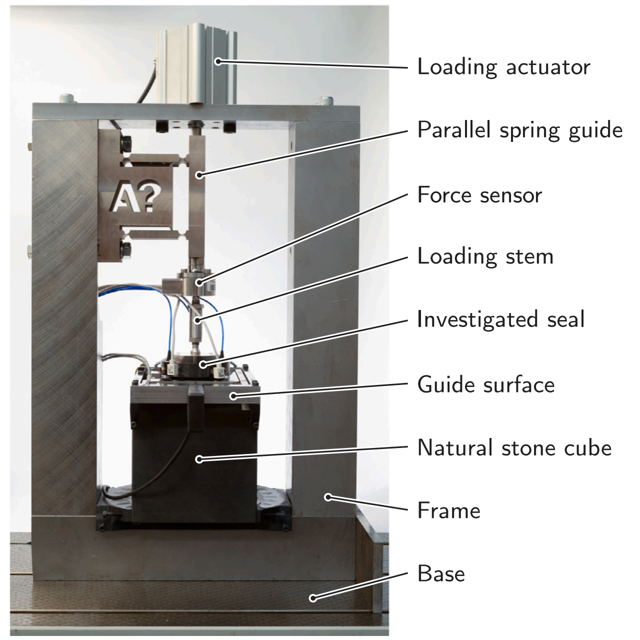

Fig. 4. Measurement setup.

The experimental setup (Fig. 4) has been developed in previous research by the authors [6,44]. In the present study, the experimental setup was further improved by integrating the air gap height sensor holder into the body of the seal and by reducing the deformations of the seal with increased stiffness and including an intermediate load spreader. This shortens the measurement loop by removing the separate sensor holder component, reducing potential sources of uncertainty. The investigated seal was loaded through a spherical joint to mitigate influence of tilting moment on the performance of the seal. A spherical joint was considered sufficient as the loading mechanism was constrained to a single degree of freedom motion with a parallel spring guide. A disk supported from its edge was used to transfer the external point load exerted on the ball socket onto a larger diameter. The load spreader reduces the deformation of the seal body under load, resulting in a more uniform air gap height in radial direction.

The air gap height and the tilt of the seal was measured with three capacitive sensors positioned at equidistant spacing on a 77 mm diameter circle. The condition with no air supply was used as the reference for zero gap height and tilt. The gap height is an average of the three sensor readings. The tilt is calculated with trigonometry from the three sensor readings.

The measurement components of the experimental setup are presented in Fig. 5. Micro-Epsilon CSH02 capacitive sensors were used for the gap height measurement. The air gap pressure was measured with pressure sensors embedded into the guide surface of the seal. The diameter of the pressure measurement hole was 0.1 mm. SMC PSE540A sensors were used to measure the pressure in the gap, the supply grooves, and the chamber of the seal. The guide surface was displaced step-wise under the seal to measure the radial pressure distribution. Seal supply flow rate was measured with SMC PF2M705 sensor and chamber flow rate was measured with two SMC PF2M705 sensors in opposing directions in order to measure flows in both directions. A stepper motor and a lead screw were used to move the guide surface, and a Heidenhain MT-25 length gauge was used to measure the displacement. A 10 kN HBM U2B force sensor was used to measure the load exerted on the seal. More detailed information on the measurement setup has been published in the previous research [6].

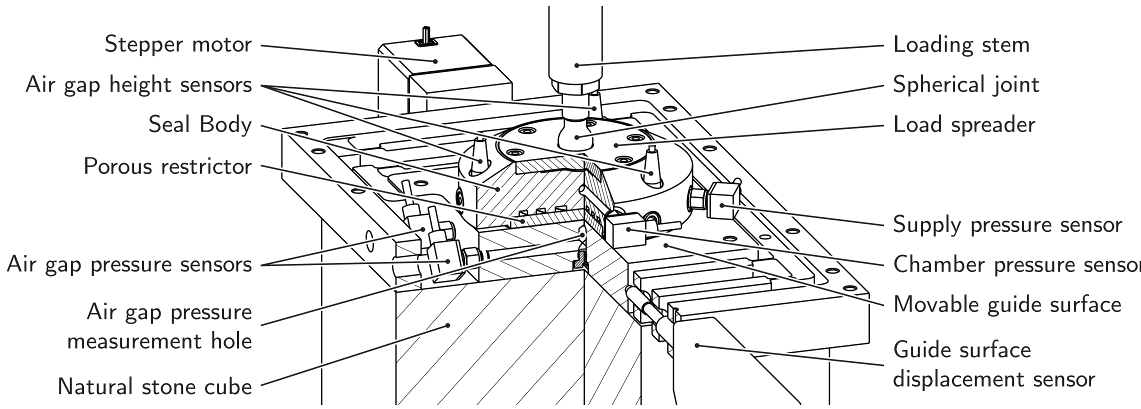

Fig. 5. Investigated seal in the measurement setup. Air gap pressure was measured with pressure sensors embedded in the guide surface that are connected to the air gap with a small hole. Seal supply pressure and chamber pressure were measured directly with sensors connected to the seal body.

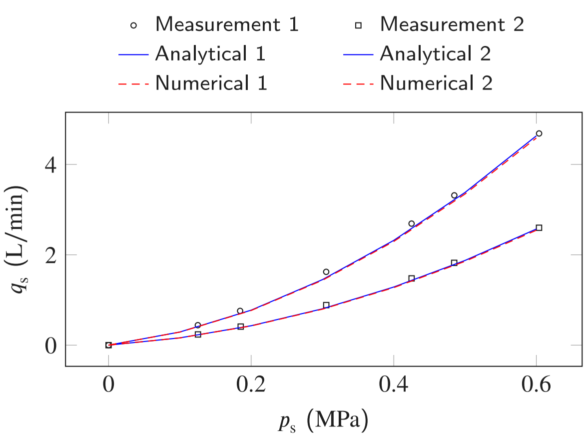

Fig. 6. Short circuit supply flow rate q_s of the investigated seals, i.e., flow rate with infinite gap height. Permeability κ of seal 1 was $9.65 \times 10^{-16}\,\mathrm{m}^2$ and permeability of seal 2 was $5.36 \times 10^{-16}\,\mathrm{m}^2$, obtained with Eq. (22) from short circuit flow rate with 0.6 MPa seal supply pressure p_s.

4. Results and discussion

4.1. Seal permeability

The permeabilities of the investigated seals were determined from measurements of short circuit flow, i.e., flow into ambient without a gap restriction. Fig. 6 presents the measured short circuit flow. Analytical and numerical model fits are shown in addition to the measurement results. The measured permeability of seal 1 was $9.65 \times 10^{-16}\,\mathrm{m}^2$ and permeability of seal 2 was $5.36 \times 10^{-16}\,\mathrm{m}^2$. Measurement with two seals with restrictors of distinct permeabilities is useful for confirming the validity of the nondimensionalization, as the nondimensional performances should be the same despite the difference in the permeability of the seals. The measured permeabilities were used in the modeling and in the nondimensialization of the experimental results.

4.2. Experimental validation

Fig. 7 presents a sample of the dimensional measurement results with results of the analytical model. The set points of the load, supply pressure and the chamber pressure were the same for measurements of both investigated seals. The analytical results, represented with red (seal 1) and blue (seal 2) lines, are with the same mean load as the corresponding measurement. In the measurements, the guide surface with the embedded air gap pressure was displaced step wise from the inner radius to the outer radius of the seal. At each radial position, the measurement consisted of 2000 samples. The mean values with error bars representing the standard deviation are presented.

Fig. 7 shows that the displacement of the guide surface has minimal effects on the load (a), stiffness (b), gap height (c), tilt (d) and flows (e), and pressures (f), validating the feasibility of the measurement method with movable guide surface. The tilting of the seal during the measurements was minimal, signifying that the experimental setup introduced minimal moment loads on the seal, and further highlighting the feasibility of the movable guide surface as part of the experimental setup. Tilting of the seal was not included in the model, as uniform gap height was assumed, thus only experimental tilt is presented in (d).

The results presented in Fig. 7 highlight the effect of the permeability on the performance of the seal. The load w (a) and the radial pressure profile in the air gap $\boldsymbol{p}$ (f) were very similar for both seals, as the set point of the load was the same in both measurements. However, the larger permeability of seal 1 (blue) results in higher flow (e), gap height (c), and lower stiffness (b) than those of the seal with smaller permeability of seal 2 (red).

In addition to measurements in spatial domain (radial position), time domain measurements were made to investigate the stability of the seal. Fig. 8 presents the vibration amplitudes in rigid body tilting mode of the seal. Fig. 8(a) presents the spectra of the seal tilt with the peak amplitude at the natural frequency of the seal tilt highlighted with a red line. The seal load-gap relation, presented in Fig. 8(d), shows that the experimental results follow theory in the load range of approximately 0.8 kN to 1.2 kN with supply pressure p_s of 0.4 MPa and chamber pressure p_c of 0.6 MPa. At lower loads the seal becomes unstable, while at higher loads the seal contacts the guide surface. At high loads, where the air gap collapses, vibration occurs at 155 Hz. At low loads, the vibration occurs at approximately 100 Hz. Further, increased vibration amplitudes are visible at loads smaller than 0.65 kN. The highlighted peak amplitude at the first natural frequency is additionally presented in (b). The bearing contacts the guide surface at loads larger than 1.2 kN, resulting in the mean tilt (c) and gap height (d) diminishing to zero while the tilt amplitude at the natural frequency slightly increases.

4.3. Effect of supply and chamber pressures

Fig. 9 presents the experimental and theoretical pressure in the air gap at supply pressures P_s of 2.97, 4.95 and 6.92 and chamber pressures P_c of 1, 2.97, 4.95 and 6.92. Theoretical results include analytical and numerical results with and without slip effects. Slip coefficient α of 0.1 was used, as has been previously used with graphite restrictors with good results [9]. The analytical and numerical results are at the feed number β of 50. The experimental results are with feed numbers in the range of 45 to 55 as the experiments were conducted with set load in contrast to set gap height. The feeding numbers correspond to gap

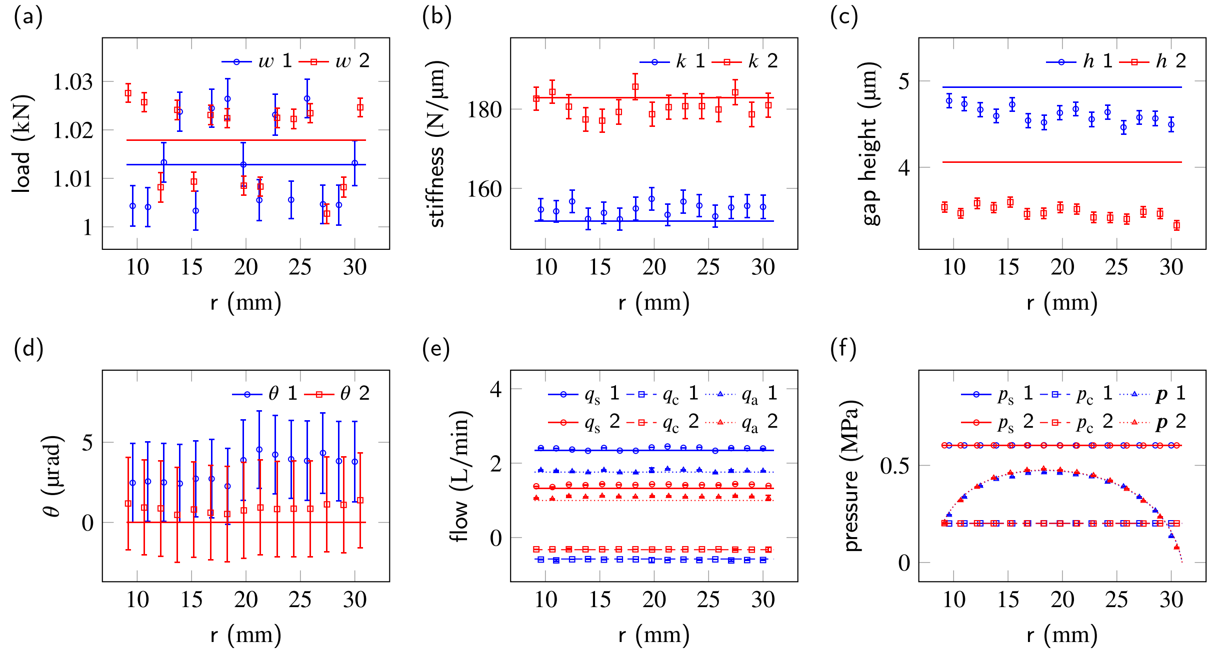

Fig. 7. Performance parameters measured step-wise from inner radius to outer radius of investigated seals 1 (blue) and 2 (red). Load w in (a); Stiffness k in (b); gap height h in (c); tilt θ in (d); supply q_s, chamber q_c, and ambient q_a flows in (e); and supply p_s, chamber p_c, and air gap $\boldsymbol{p}$ pressures in (f). Each marker is a mean of 2000 samples at a measurement position with error bars showing the standard deviation of the samples. Lines show the results of analytical model with no slip with same mean gap height, supply pressure and chamber pressure as the corresponding measurement.

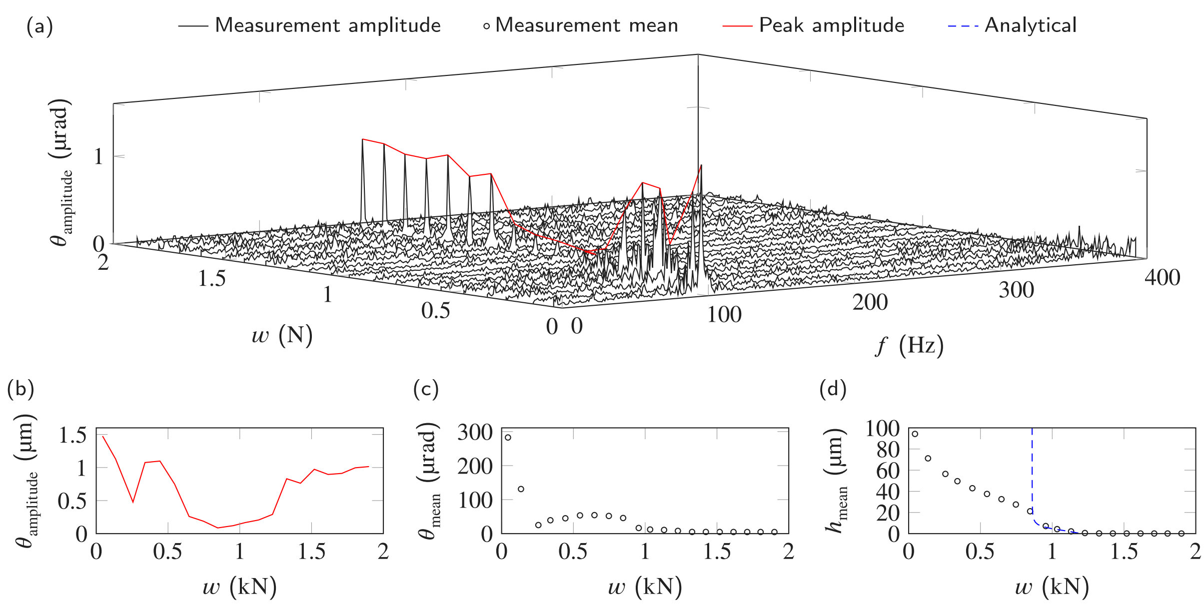

Fig. 8. Experimental tilt amplitude spectra (a), peak tilt amplitude (b), mean tilt (c), and mean gap height (d) of seal 1 in relation to the load w with supply pressure $p_s = 0.4$ MPa and chamber pressure $p_c = 0.6$ MPa. Peak vibration amplitude (red line) was at rigid body tilt mode of the seal occurs at 100 Hz to 155 Hz, depending on the load.

heights of approximately 2.9 µm with seal 1 and of 2.5 µm with seal 2. Measurements at $P_s = 2.97$ and $P_c = 6.92$ were not possible due to the instability of the seals, as the seal was either in at very small (<0.5 µm) gap height or at a large (>25 µm) gap height depending on the load. No stable gap height could be achieved in between these ranges with either increasing or decreasing loading.

The experimental and theoretical results show good correlation especially with lower pressure differences across the seal. The measured pressures in the air gap for seal 2 at mainly supply pressure P_s of 2.97 are lower than the theoretical and the measurements of seal 1. As is expected, the numerical results have slightly better correlation with the experiments than the analytical model. However, the difference between the numerical and the analytical model is small.

Performance of the investigated seal in relation to the porous feeding number β with supply pressure P_s of 6.92 and chamber pressure P_c of 1 is presented in Fig. 10. Theoretical and experimental results of load capacity (a), static stiffness (b), supply mass flow (c), chamber mass flow (d), and ambient mass flow (e) are presented. Additionally, the tilt of the seal in the experiments is presented in (f). The tilt of the seal is negligible for majority of the measured feeding number β range, only increasing at small values of β (large gap height). Nondimensionalized experimental results with feeding number β in the range of 0.5 to 250

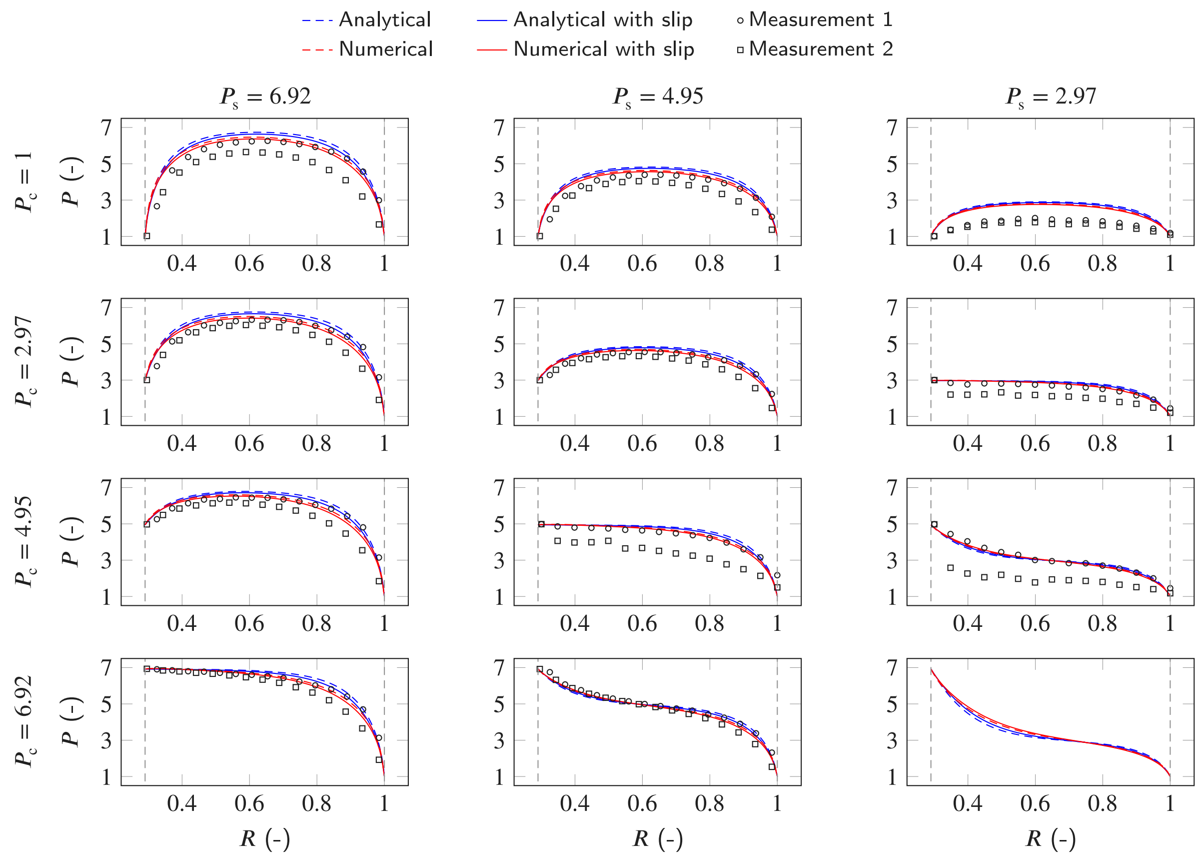

Fig. 9. Seal gap pressure distributions with varying supply pressure P_s and chamber pressure P_c at feeding number β of 50, corresponding to gap height of 2.9 µm with seal 1 and to gap height of 2.5 µm with seal 2. Gray vertical dashed lines highlight the inner radius at $R = 0.29$ and the outer radius at $R = 1$ of the investigated seal. Measurements at $P_s = 2.97$ and $P_c = 6.92$ were not possible due to instability of the seals.

are presented. The feeding number range corresponds to gap heights of 13.6 µm to 1.7 µm for seal 1 and 11.3 µm to 1.4 µm are presented.

Mass flows of the investigated seal are presented in 10 (c), (d) and (e). For the mass flows, positive flow direction is towards increasing radius. Thus, negative chamber flows mean flow towards the chamber at the centre of the seal. The theoretical mass flows are slightly smaller than that of the measurements for the three flows. Presumably, some of the difference can be attributed to errors in the geometry of the seal, i.e., flatness errors resulting in larger gap heights.

Fig. 11 presents the performance results of the analytical no-slip model with varying seal supply P_s and chamber P_c pressures. Fig. 11 (b) shows that the static stiffness of the seal increases with increasing supply pressure, and decreases with increasing chamber pressure. Under conditions where the air gap pressure is significantly lower than the pressure in the chamber, the seal becomes unstable. The static stiffness of the seal is negative at the combination of the lowest investigated supply pressure P_s of 2.97 and the highest investigated chamber pressure P_c of 6.92, as was seen in the pressure distributions of Fig. 9. Furthermore, the seal supply mass flow reverses at that supply and chamber pressure combination (Fig. 11 (c)). This instability is the cause why the pressure distribution measurements (Fig. 9) were not possible at that pressure combination.

4.4. Effect of seal width

The effect of the seal width, i.e., the diameter ratio R_c/R_a was investigated theoretically with the analytical model. The analytical model was used as it disregards any effects of the supply groove geometry, which were included in the numerical model. Performance contours at supply pressure P_s of 4.95 and chamber pressure P_c of 1 to 6.92 are presented in Fig. 12. The pressure levels were selected to have chamber pressures lower, equal, and higher than the chamber pressure in order to highlight the existence of no-leakage and leakage conditions.

The width of the seal width mainly effects the stiffness and the leakage of the seal. For very thin seals, where $R_c/R_a \to 1$, the load capacity (a) and stiffness (b) and the supply mass flow (c) diminish. The effect is more pronounced at smaller feeding numbers (larger gap heights), as the flow restriction in the gap is lower.

The ratio between the seal supply pressure P_s and chamber pressure P_c has an dominant effect on the stiffness (b) and the chamber leakage (d) of the seal. Feasible operating conditions with low leakage and reasonable stiffness are achieved when the supply pressure is larger than the chamber pressure and the preload of the seal is such that the seal operates at or near the peak stiffness (red curves, feeding number β of 1 to 100). Moreover, higher chamber pressure than the seal supply pressure has detrimental impact on the stiffness and leakage of the seal, particularly at smaller feeding numbers (larger gap heights).

5. Conclusions

This research proposes a analytical solution to the modified Reynolds equation for annular aerostatic seals. The analytic solution is compared to a numerical model and to experimental results of two 64 mm seals. The analytical model assumes one dimensional flow in the restrictor and a gas supply that spans the whole restrictor, drastically reducing the complexity of the porous feeding of the modified Reynolds equation. The numerical model assumes two dimensional flow in the restrictor and includes the geometry of the gas supply. Thus, the numerical model represents more accurately the pressure distribution in the porous restrictor. The results are presented in nondimensional form for applicability to general problems, using a proposed normalization scheme for porous aerostatic seals.

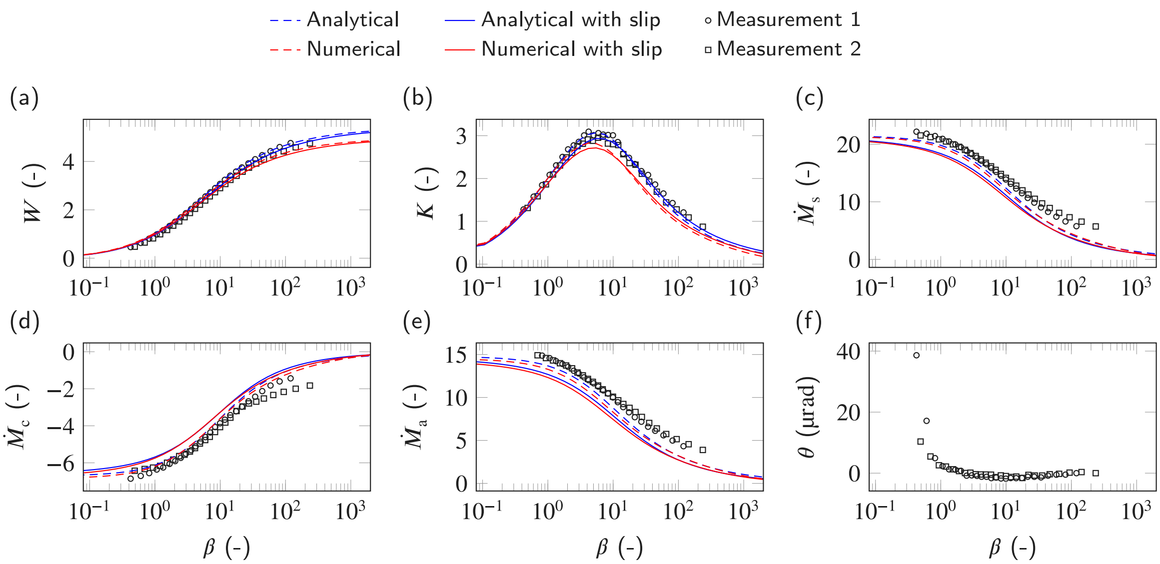

Fig. 10. Load (a); stiffness (b); supply (c), chamber (d), and ambient (e) mass flows; and tilt (f) with supply pressure P_s of 6.92 and chamber pressure P_c of 1. Feeding parameter β is inversely proportional to the cube of gap height h.

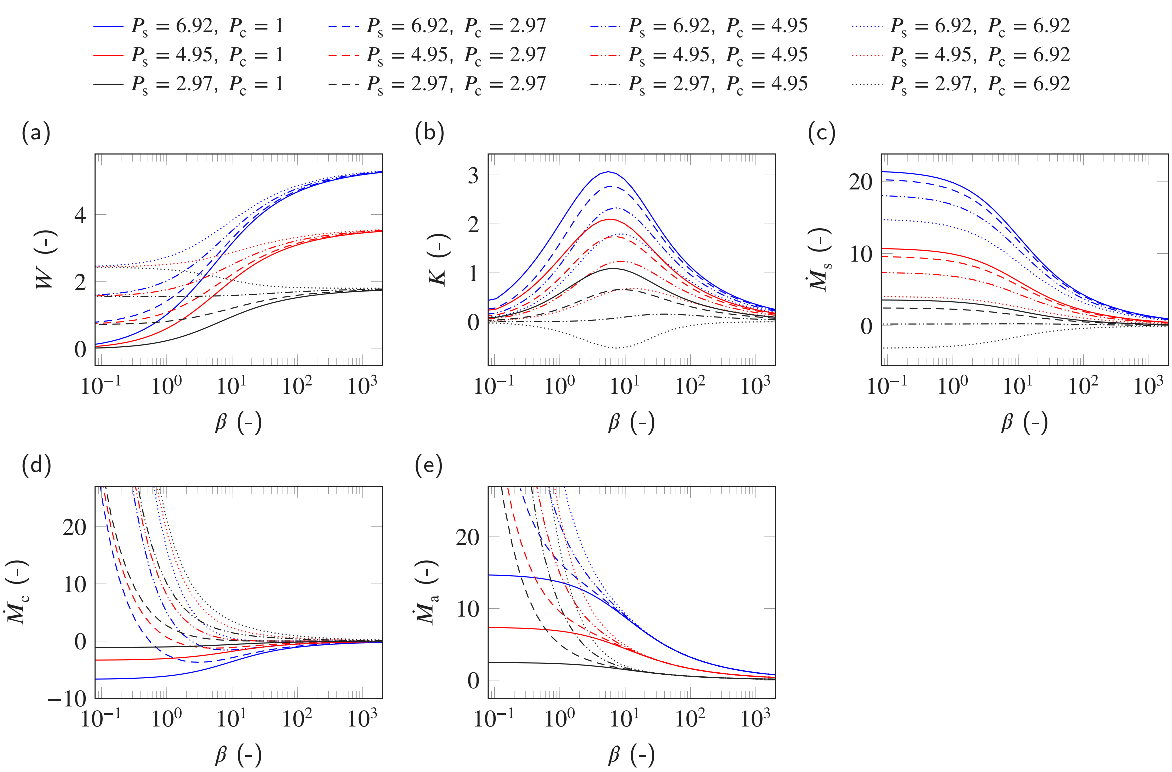

Fig. 11. Seal performance: load (a); stiffness (b); and supply (c), chamber (d), and ambient (e) mass flows. Analytical no-slip model, various seal supply P_s and chamber P_c pressures.

It is shown, that under static conditions the proposed analytical solution is equal to the numerical solution and the experiments in terms of the key performance metrics of air gap pressure distribution, load capacity, stiffness and mass flows. Further, the effect of slip at the interface between the porous restrictor and air gap are small under the static conditions of this research. These results corroborates feasibility of the proposed analytical solution for aerostatic seals.

This study also investigated performance of the aerostatic seals with varying operational parameters, including the seal supply pressure and the chamber pressure. The theoretical results show that aerostatic seal can have negative static stiffness in conditions where the peak pressure in the air gap is lower than the pressure of the high-pressure side of the seal. This instability was also demonstrated in the experiments at supply pressure P_s of 0.297 and chamber pressure P_c of 6.92. The static stiffness of the seal increases by increasing the supply pressure and by reducing the chamber pressure, i.e., by reducing the pressure difference across the seal. The increase of supply pressure is at the cost of higher supply gas consumption. Furthermore, the width of the seal has an

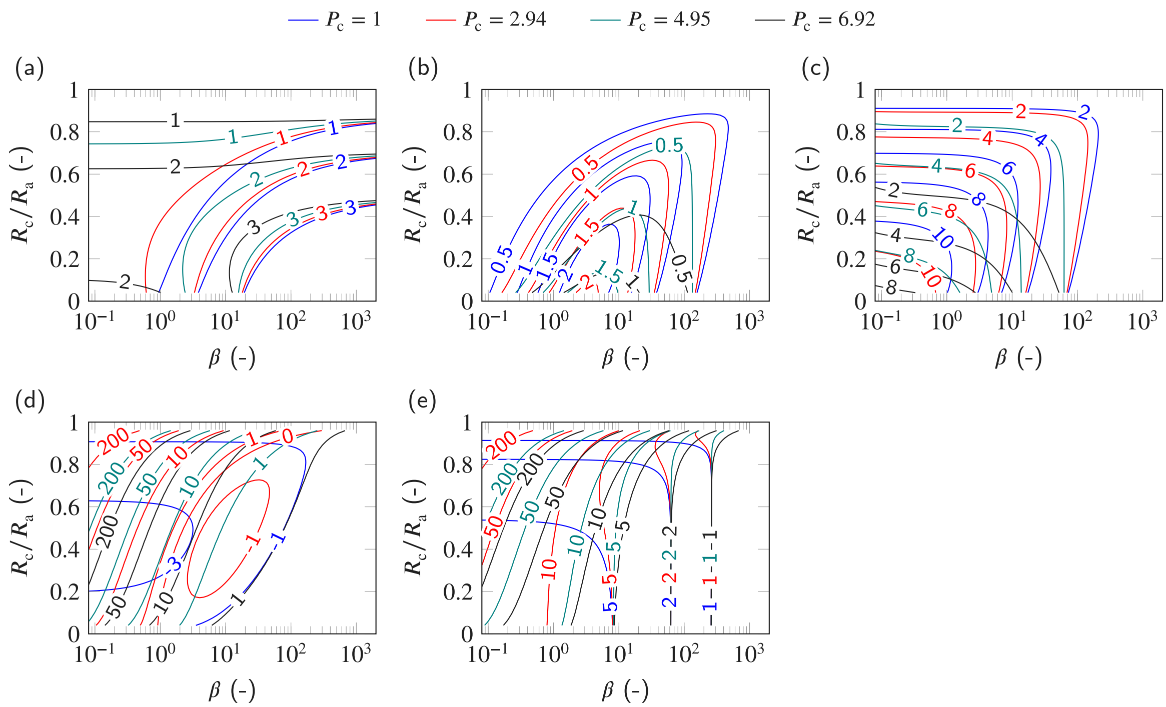

Fig. 12. Effect of seal width, i.e., ratio R_c/R_a, on load W (a), stiffness K (b), supply mass flow $\dot{M}_s$ (c), chamber mass flow $\dot{M}_c$ (d) and ambient mass flow $\dot{M}_a$ (e). Analytical no-slip model, supply pressure $P_s = 4.95$ and various chamber P_c pressures.

influence on stiffness and leakage, wider seals are more stiff and have smaller leakage than narrow seals.

CRediT authorship contribution statement

Mikael Miettinen: Writing – original draft, Visualization, Project administration, Methodology, Investigation, Funding acquisition, Formal analysis, Conceptualization. **Valtteri Vainio:** Investigation, Funding acquisition. **Raine Viitala:** Writing – review & editing, Supervision, Funding acquisition.

Declaration of competing interest

The authors declare that they have no known competing financial interests or personal relationships that could have appeared to influence the work reported in this paper.

Data availability

Data will be made available on request.

Acknowledgments

The research was funded by Business Finland (Power Beyond, grant number 2534/31/2022).

References

[1] Schoar S, Dohmen HJ, Benra F-K. Reliable seals for turbomachines: numerical analysis of the effects of compressible fluid flow through porous materials and narrow gaps. In: Proceedings of 13th European conference on turbomachinery fluid dynamics & thermodynamics. 2019, p. 1–11. http://dx.doi.org/10.29008/ETC2019-303, URL: http://www.euroturbo.eu/publications/proceedings-papers/ETC2019-303/.

[2] Schoar S, Elspaß A, Kleszczynski S, Dohmen HJ, Benra F-K. Validation of a numerical model to support the design of additively manufactured aerostatic dry gas seals carried out on a test bench through use of seals with defined permeabilities. In: Proceedings of 14th European conference on turbomachinery fluid dynamics & thermodynamics. 2021, p. 1–12. http://dx.doi.org/10.29008/ETC2021-541, URL: https://www.euroturbo.eu/publications/proceedings-papers/ETC2021-541/.

[3] Schoar S, Elspaß A, Dohmen HJ, Kleszczynski S, Benra F-K. Design and fabrication of optimized aerostatic dry gas seals using advanced numerical models and next generation production technology. Polytech Des 2021;9(3):156–66. http://dx.doi.org/10.19279/TVZ.PD.2021-9-3-11.

[4] Schoar S. Experimentelle und numerische untersuchungen des einsatzes von materialien mit definierten durchlässigkeitsbeiwerten und deren verteilung in aerostatisch wirkenden gasdichtungen (Ph.D. thesis), Universität Duisburg-Essen; 2021, http://dx.doi.org/10.17185/duepublico/75397, URL: https://duepublico2.uni-due.de/receive/duepublico_mods_00075397.

[5] Miettinen M, Vainio V, Theska R, Viitala R. Aerostatically sealed chamber as a robust aerostatic bearing. Tribol Int 2022;173:107614. http://dx.doi.org/10.1016/j.triboint.2022.107614, URL: https://www.sciencedirect.com/science/article/pii/S0301679X22001876.

[6] Miettinen M, Vainio V, Theska R, Viitala R. On the static performance of aerostatic elements. Precis Eng 2024;89:1–10. http://dx.doi.org/10.1016/j.precisioneng.2024.05.017.

[7] Jiang S, Yang S, Yin Z, Xu C. Static and dynamic characteristics of externally pressurized annular porous gas thrust bearings. Proc Inst Mech Eng J: J Eng Tribol 2016;230:1221–30. http://dx.doi.org/10.1177/1350650116631275, URL: http://journals.sagepub.com/doi/10.1177/1350650116631275.

[8] Cappa S, Reynaerts D, Al-Bender F. Reducing the radial error motion of an aerostatic journal bearing to a nanometre level: Theoretical modelling. Tribol Lett 2014;53:27–41. http://dx.doi.org/10.1007/s11249-013-0241-8, URL: http://link.springer.com/10.1007/s11249-013-0241-8.

[9] Cappa S. Reducing the error motion of an aerostatic rotary table to the nanometre level (Ph.D. thesis), Faculty of Engineering Science; 2014, p. 230.

[10] Cui C, Ono K. Theoretical and experimental investigation of an externally pressurized porous annular thrust gas bearing and its optimal design. J Tribol 1997;119(3):486–92. http://dx.doi.org/10.1115/1.2833524.

[11] Al-Bender F. Air bearings - theory, design and applications. John Wiley & Sons; 2021, p. 592.

[12] Rasnick WH, Arehart TA, Littleton DE, Steger PJ. Porous graphite air-bearing components as applied to machine tools. Technical report, Dearborn: Society of manufacturing engineers; 1974, URL: https://www.osti.gov/servlets/purl/5110726.

[13] Lee CC, You HI. Geometrical design considerations on externally pressurized porous gas bearings. Tribol Trans 2010;53(3):386–91. http://dx.doi.org/10.1080/10402000903312380.

[14] Lee C-C, You H-I. Characteristics of externally pressurized porous gas bearings considering structure permeability. Tribol Trans 2009;52(6):768–76. http://dx.doi.org/10.1080/10402000903097403.

[15] Nicoletti R, Silveira ZC, Purquerio BM. Modified Reynolds equation for aerostatic porous radial bearings with quadratic forchheimer pressure-flow assumption. J Tribol 2008;130:1–12. http://dx.doi.org/10.1115/1.2919776, URL: https://asmedigitalcollection.asme.org/tribology/article/130/3/031701/468576/Modified-Reynolds-Equation-for-Aerostatic-Porous.

[16] Luong TS, Potze W, Post JB, Van Ostayen RA, Van Beek A. Numerical and experimental analysis of aerostatic thrust bearings with porous restrictors. Tribol Int 2004;37(10):825–32. http://dx.doi.org/10.1016/j.triboint.2004.05.004.

[17] Cieslicki K. Investigations of the effect of inertia on flow of air through porous bearing sleeves. Wear 1994;172(1):73–8. http://dx.doi.org/10.1016/0043-1648(94)90301-8.

[18] Cui J, You X, Zhang H, Liu J. Permeability prediction of porous aerostatic bearings through 3D morphology and fractal calculation method. Int J Appl Ceram Technol 2024. http://dx.doi.org/10.1111/ijac.14702.

[19] Zeng C, Wang W. Modeling method for variable and isotropic permeability design of porous material based on TPMS lattices. Tribol Int 2022;176. http://dx.doi.org/10.1016/j.triboint.2022.107913.

[20] Zeng C, Wang W, Cheng X, Zhao R, Cui H. Three-dimensional flow state analysis of microstructures of porous graphite restrictor in aerostatic bearings. Tribol Int 2021;159. http://dx.doi.org/10.1016/j.triboint.2021.106955.

[21] Cui H, Wang Y, Yue X, Huang M, Wang W. Effects of manufacturing errors on the static characteristics of aerostatic journal bearings with porous restrictor. Tribol Int 2017;115(April):246–60. http://dx.doi.org/10.1016/j.triboint.2017.05.008.

[22] Cui H, Wang Y, Zhang M, Wang W, Zhao C. A fractal method to calculate the permeability for compressible gas flow through a porous restrictor in aerostatic bearings. Int J Heat Mass Transfer 2018;121:437–52. http://dx.doi.org/10.1016/j.ijheatmasstransfer.2018.01.012.

[23] Cui H, Wang Y, Yue X, Li Y, Jiang Z. Numerical analysis of the dynamic performance of aerostatic thrust bearings with different restrictors. J Eng Tribol 2019;233(3):406–23. http://dx.doi.org/10.1177/1350650118780599.

[24] Hosokawa T, Somaya K, Miyatake M, Yoshimoto S. Static characteristics of aerostatic thrust bearings with multiple porous inlet ports. J Tribol 2015;137. http://dx.doi.org/10.1115/1.4028999, URL: https://asmedigitalcollection.asme.org/tribology/article/doi/10.1115/1.4028999/442591/Static-Characteristics-of-Aerostatic-Thrust.

[25] Sahto MP, Wang W, Sanjrani AN, Hao C, Shah SA. Dynamic performance of partially orifice porous aerostatic thrust bearing. Micromachines 2021;12(8):1–23. http://dx.doi.org/10.3390/mi12080989.

[26] Cracaoanu I, Bremer F. Air bearings in high precision systems. Int J Sustain Constr Des 2014;4(2). http://dx.doi.org/10.21825/scad.v4i2.1041.

[27] Li W, Wang S, Feng K. Numerical and experimental study on the effect of surface damages on the performances of porous aerostatic bearings. Tribol Int 2022;175:107791. http://dx.doi.org/10.1016/j.triboint.2022.107791, URL: https://linkinghub.elsevier.com/retrieve/pii/S0301679X22003644.

[28] Beavers GS, Sparrow EM, Masha BA. Boundary condition at a porous surface which bounds a fluid flow. AIChE J 1974;20:596–7. http://dx.doi.org/10.1002/aic.690200323.

[29] Goldstein ME, Braun WH. Effect of velocity slip at a porous boundary on the performance of an incompressible porous bearing. Technical teport TN D-6181, NASA; 1971.

[30] Saffman PG. On the boundary condition at the surface of a porous medium. Stud Appl Math 1971;50(2):93–101. http://dx.doi.org/10.1002/sapm197150293.

[31] Beavers GS, Sparrow EM, Magnuson RA. Experiments on coupled parallel flows in a channel and a bounding porous medium. J Basic Eng 1970;92:843–8. http://dx.doi.org/10.1115/1.3425155.

[32] Beavers GS, Joseph DD. Boundary conditions at a naturally permeable wall. J Fluid Mech 1967;30:197–207. http://dx.doi.org/10.1017/S0022112067001375.

[33] Ishizawa S, Hori E. The flow of a viscous fluid through a porous wall into a narrow gap : A consideration of the slip of fluid on a porous wall surface. Bull JSME 1966;9:719–30. http://dx.doi.org/10.1299/jsme1958.9.719, URL: http://www.jstage.jst.go.jp/article/jsme1958/9/36/9_36_719/_article.

[34] Sparrow EM, Beavers GS, Hwang IT. Effect of velocity slip on porous-walled squeeze films. J Lubr Technol 1972;94:260–4. http://dx.doi.org/10.1115/1.3451704, URL: https://asmedigitalcollection.asme.org/tribology/article/94/3/260/429397/Effect-of-Velocity-Slip-on-PorousWalled-Squeeze.

[35] Majumder M, Majumder B. Study of the pneumatic instability of externally pressurized porous gas thrust bearings with slip velocity. Wear 1988;124(3):261–77. http://dx.doi.org/10.1016/0043-1648(88)90217-7, URL: https://linkinghub.elsevier.com/retrieve/pii/0043164888902177.

[36] Zhang X, Ding S, Du F, Ji F, Xu Z, Liu J, Zhang Q, Zhou Y. Investigation into gas lubrication performance of porous gas bearing considering velocity slip boundary condition. Friction 2022;10:891–910. http://dx.doi.org/10.1007/s40544-021-0503-7.

[37] Constantinescu VN. Gas lubrication. American Society of Mechanical Engineers; 1969, p. 621, URL: https://archive.org/details/gaslubrication0000cons/page/46/mode/2up.

[38] Sun D-C. Stability analysis of an externally pressurized gas-lubricated porous thrust bearing. J Lubr Technol 1973;95:457–68. http://dx.doi.org/10.1115/1.3451857, URL: https://asmedigitalcollection.asme.org/tribology/article/95/4/457/418080/Stability-Analysis-of-an-Externally-Pressurized.

[39] Murti PR. Squeeze films in porous circular disks. Wear 1973;23:283–9. http://dx.doi.org/10.1016/0043-1648(73)90017-3.

[40] Murti PRK. Analysis of externally pressurized gas porous bearings. J Lubr Technol 1974;96:354–60. http://dx.doi.org/10.1115/1.3451963, URL: https://asmedigitalcollection.asme.org/tribology/article/96/3/354/418540/Analysis-of-Externally-Pressurized-Gas-Porous.

[41] Sun D-C. On the stiffness and damping properties of an externally pressurized, gas-lubricated porous thrust bearing. In: Proceedings of the 7th international gas bearing symposium. 1976, p. 67–81.

[42] Gao Q, Chen W, Lu L, Huo D, Cheng K. Aerostatic bearings design and analysis with the application to precision engineering: State-of-the-art and future perspectives. Tribol Int 2019;135:1–17. http://dx.doi.org/10.1016/j.triboint.2019.02.020.

[43] Majumdar BC. Dynamic characteristics of externally pressurized rectangular porous gas thrust bearings. J Lubr Technol 1976;98(1):181–6. http://dx.doi.org/10.1115/1.3452762, URL: https://asmedigitalcollection.asme.org/tribology/article/98/1/181/418631/Dynamic-Characteristics-of-Externally-Pressurized.

[44] Vainio V, Miettinen M, Majuri J, Theska R, Viitala R. Manufacturing and static performance of porous aerostatic bearings. Precis Eng 2023;84:177–90. http://dx.doi.org/10.1016/j.precisioneng.2023.06.014, URL: https://www.sciencedirect.com/science/article/pii/S0141635923001265.

Mikael Miettinen received his B.Sc. (Tech.) and M.Sc. (Tech.) degrees in mechanical engineering from Aalto University in Espoo, Finland, in 2019 and 2020, respectively. He is currently pursuing a D.Sc. (Tech.) degree in mechanical engineering at the same institution. His current research topics include externally pressurized porous gas bearings and seals, particularly in the context of applications in large rotors.

Valtteri Vainio was born in 1995. He has received his M.Sc. degree in mechanical engineering from Aalto University in 2021. Currently, he is pursuing a D.Sc. degree in mechanical engineering at Aalto University. In his master's thesis he investigated the manufacturing and performance measurement of porous material aerostatic bearings. Current research topics include porous aerostatic bearings with focus on manufacturing methods.

Raine Viitala was born in 1992. He received his M.Sc. and D.Sc. degrees in mechanical engineering from Aalto University in 2017 and 2018, and was appointed Assistant Professor in 2020. His doctoral dissertation was acknowledged with the Aalto University School of Engineering dissertation award. In 2018, Viitala visited Technische Universität Darmstadt researching rotating kinetic energy storages, i.e., flywheels. Viitala has a solid background in experimental large rotor research, including vibration analysis, bearing excitations, roundness measurements and manufacturing for operating conditions. His work is widely applied in several industrial applications, such as electric motors and generators, turbines, and paper machines. He is instructing students at all academic levels, and is the responsible teacher of Mechatronics minor at Aalto University.